scientific reports

OPEN

Defect engineering in organic semiconductor based metal-dielectric photonic crystals

Khadga S. Thakuri[1], Thomas Cleary[1], David Allemeier[2,3], Taisei Kimura[4], Naoya Aizawa[5], Ken-ichi Nakayama[5], Akito Masuhara[4] & Matthew S. White[1,2]✉

We investigate the band structure of metal-dielectric photonic crystals comprising stacked organic semiconductor microcavities with silver metal mirrors incorporating crystal defects: individual unit cells with aperiodic dimensionality. Both transfer matrix simulation and experimental verification are performed to investigate the impact on the photonic band structure as a single cavity is varied in size. The resulting mid-gap defect states are shown to hybridize with a photonic band at certain resonant dimensions. The resonance of the defect cavity affects the transmittance of light through the device, disrupting or enhancing the coupling between otherwise resonant cavities. We outline potential applications for defect engineering of these devices through controlled manipulation of the transmission spectrum.

Photonic crystals (PCs) are nanostructures with periodic interfaces between materials with distinct index of refraction (n) and extinction coefficient (κ). The emergence of a photonic band gap, analogous to the forbidden energy gap of an electronic band structure in a solid, is a key feature of these structures[1–4]. PC structures have received much interest in nanophotonics due to their ability to control and manipulate light, leading to the development of advanced optical components and devices with applications spanning sensing[5,6], telecommunications[7,8], laser technology[9,10], chemical, biological, and medical research fields[11–15].

Heterogeneous dielectric interfaces are the most common unit cells in PCs, but metal-dielectric interfaces incorporated in the periodicity of PC structures result in a subclass of hybrid PC structures called metal-dielectric photonic crystals (MDPCs). The hybrid MDPC structures offer interesting features such as polarization-insensitive optical resonances[16], capability to support Fabry-Pérot resonances[17], high local electric field and strong non-linear effects[18,19], and Epsilon-Near-Zero crystals[20]. Electroluminescent organic materials may be incorporated into MDPC structures, employing microcavity organic light emitting diodes (OLED) as unit cells to create MDPC OLEDs[21,22] which exhibit many of the properties of a PC and also function as an electroluminescent device. Our previous work on 1-D MDPC OLEDs demonstrates a correlation between material composition[22] and physical dimensions[21,23] of the MDPCs with features of the photonic band structure including the number, energies, and linewidths of states in the band and an asymmetry-induced Peierls bandgap. Building on this foundation, our current study shifts focus to passive MDPC configuration, distinct from the electroluminescent MDPC OLEDs. Here we utilize a single layer of organic material as an optical spacer between two metallic layers, which define a microcavity as the unit cell of the MDPC structure. This approach enables us to gain clearer insights into the underlying behavior of MDPCs in the discrete regime eliminating the additional complexity of electroluminescence, such as emitter-cavity coupling, thermal management, and the necessity to balance electron and hole transport in the device.[24]

The inclusion of a geometric defect in the MDPC structures is analogous to impurity doping in semiconductors and may enable a further degree of control over the photonic band structure through mid-gap energy states.[25–27] Such defects can be introduced by manipulating the size, shape, or arrangement of the constituent components of the photonic crystal lattice. Here we insert the geometrical defect in the MDPC by detuning the thickness of a single unit cell within the crystal. In this work, we conduct transfer matrix simulations to demonstrate the creation and control of defect states in the photonic band gap of 1-D MDPC structures and experimentally verify

[1]Department of Physics, The University of Vermont, Burlington, VT 05405, USA. [2]Material Science Program, The University of Vermont, Burlington, VT 05405, USA. [3]Department of Mechanical Engineering, Boston University, Boston, MA 02215, USA. [4]Graduate School of Science and Engineering, Yamagata University, Yonezawa, Yamagata 992-8510, Japan. [5]Division of Applied Chemistry, Graduate School of Engineering, Osaka University, Suita, Osaka 565-0871, Japan. ✉email: mwhite25@uvm.edu

by fabricating organic-semiconductor-based MDPCs. We show that the density of states in the band can be controlled by tuning the geometry of the device and the location of defects within the microcavity stack. Defect engineering emerges as a powerful tool for shaping the emission spectra of MDPCs for isolating individual spectral peaks and for suppressing or enhancing the coupling between resonant cavities within the crystal.

MDPC structures and methods

For the purposes of this work we use $N = 3$ stacked cavities to constitute the MDPC structure as this is the simplest structure that demonstrates the band engineering principles. The findings can be generalized to larger crystals and corresponding data for $N = 5$ MDPCs are shown in the Supplementary Information (SI). We design our MDPC structure with the arrangement of single-component dielectric layers and identical metal mirrors to achieve maximum physical and optical symmetry. For the dielectric layer, an organometallic compound Tris-(8-hydroxyquinoline) aluminum (Alq_3) is used, which is one of the widely used organic semiconductors in OLEDs, and can be use in MDPC OLEDs as well for an emitter and/or electron transport layer[21,28]. Silver (Ag) is used for both top and bottom metal layers, which act as semi-transparent mirrors and generate partial reflections. Schematic illustrations of the $N = 3$ stacked cavities MDPC device structures, with a defect introduced in the Alq_3 layer at the center and edge of the cavity, are shown in Fig. 1a,b, respectively. Figure 1c presents an SEM image of an $N = 3$ MDPC device, with standard edge cavities, each 350 nm thick,
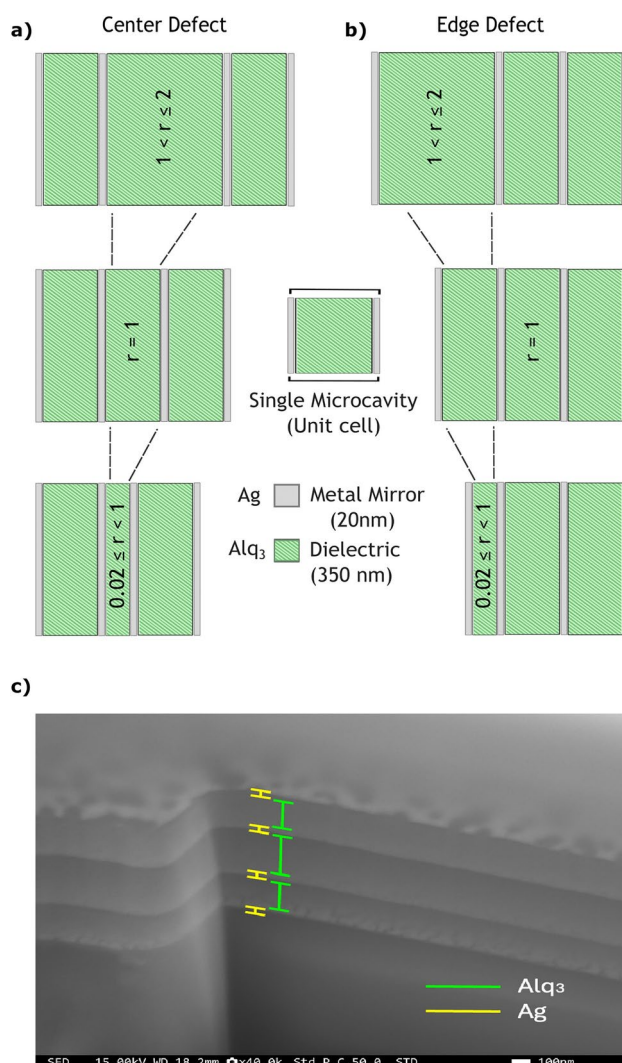

Fig. 1. Schematic representation of typical three-cavity MDPC device designed by stacking three-layer microcavity with alternating Ag and Alq_3 layers. (**a**) and (**b**) represent the schematics of MDPCs with the defect introduced in a dielectric (Alq_3) layer of center and edge cavity respectively. All mirrors are 20 nm thick and the thickness of standard or static organic layer is 350 nm. Defect percentages were varied from -98% to +100% ($0.02 \leq r \leq 2$) of standard size (350 nm) with the step of 1%. Inset shows the schematic of a single unit cell which is defined as a single microcavity. (**c**) Cross-sectional SEM image of an $N = 3$ MDPC device with $r = 1.50$ in center cavity, taken at a $45°$ angle using secondary electron detector, prepared by focused ion beam.

alongside a central cavity that is 525 nm thick ($r = 1.50$), captured from a cross-section at a $45°$ sample tilt. A 150 nm platinum layer was sputtered onto the top silver layer of the device to protect it from damage during sample preparation using focused ion beam milling. A functional OLED device may require three or four layers of organics like bathophenanthroline (BPhen) as an electron transport layer, Alq_3 as an emissive layer, and N, N'-di(1-naphthyl)-N, N'-diphenyl-(1,1'-biphenyl)-4,4'-diamine (NPB) as a hole transport layer. Additionally, interfacial injection layers like lithium fluoride (LiF) and molybdenum oxide (MoO_x) may require serving as electron and hole injection layers, along with different anode/cathode materials which can alter the band structure in predictable ways[21,22].

Device fabrication and characterization

The vertical stack of microcavity resonators was fabricated by using a thermal evaporator system from Angstrom Engineering. Both Ag (purchased from R.D.Mathis) and Alq_3 (purchased from Luminescence Technology) materials were deposited through thermal evaporation in the high vacuum (below 10^{-5} Torr). On a glass substrate, a sequential thermal evaporation process was carried out, starting with the semitransparent bottom layer of Ag metal, followed by an organic layer of Alq_3, and then repeating the same sequence, to fabricate the $N = 3$ MDPC devices. The Ag metal and Alq_3 organic layers were evaporated at rates of 1.5 Å/s and 1.0 Å/s, respectively, while the substrate holder rotated at 10 rpm to ensure uniform film thickness. The deposition rate and thickness were observed by quartz crystal monitor installed in the evaporator. The Alq_3 organic semiconductor was purified by vacuum sublimation process and the devices were stored inside a nitrogen glovebox.

Both a Cary 7000 UV-Vis-NIR and a custom-built system with an Ocean Optics HDX spectrometer and a DH-2000 UV-VIS-NIR driving light source were used to record and analyze the transmission spectra. The thicknesses of the individual metal and organic films, as well as the overall thickness of the device, were measured using a Dektak XT stylus profilometer. The optical constants n and κ are necessary input parameters to the transfer matrix model. To measure the optical constants of Alq_3, 60nm Alq_3 was deposited by thermal evaporation onto a silicon wafer with 200 nm thermal oxide. A HORIBA Jobin Yvon Spectrum Ellipsometer was used to collect the spectra and Deltapsi 2 software was used for the acquisition and treatment of ellipsometric data.

Computational predictions of the band structure for $N = 3$ MDPC structures with both center and edge cavity defects were simulated using the transfer matrix formalism technique. Such numerical results have been shown to closely reproduce the peak locations and linewidths of experimental spectra in MDPC structures.[21-23]. The transfer matrix approach accurately describes the behavior of 1-D optical systems such as 1-D MDPC structures where the electric fields on both side (left-had and right-hand) of the material stack are expressed through the transfer matrix S. S is the product of propagation matrix P and scattering matrix M where P describes the wave propagation through bulk layers of the structure, and M describes the incoming and outgoing electric fields at each interface[24]. We define two defect conditions by locating an anomalously thin or thick cavity in the center or edge position of the $N = 3$ MDPC. The center, intermediate, and edge positions are simulated for the $N = 5$ MDPC and discussed in the Supplementary Information. We defined a ratio r as:

$$r = \frac{t_d}{t_s} \qquad (1)$$

Where t_d is the thickness of the defect cavity and $t_s = 350$ nm is a standard or static cavity size. We considered a range of $0.02 \leq r \leq 2$, where the defect cavity ranges from 2% the size of the standard cavities to 200% in intervals of 1%. The 350 nm dielectric layer thickness yields two photonic bands (the second and third) within the 400-800 nm window, allowing us to observe defect band structure dynamics spanning the visible spectrum.

Results

Emergence of defect states

A MDPC with three stacked uniform cavities will exhibit photonic bands with three evenly spaced energy states[22]. The MDPCs in this work have $t_s = 350$ nm thick organic dielectric layers, resulting in photonic bands centered roughly at 483 nm and 691 nm as seen in the bottom spectrum of Fig. 2. The center of the photonic bands represent the energies of the eigenstates of a single, uncoupled microcavity resonator. In the case of a homogeneous, lossless, organic dielectric layer between identical mirrors, these eigenstates can be expressed as[29]:

$$\lambda_j = \frac{2}{[j - \phi/\pi]} n_{org} \, t_{org} \qquad j = 1, 2, 3, \ldots \qquad (2)$$

Where, λ_j is the resonance wavelength of index j, n_{org} and t_{org} are the index of refraction and thickness of the organic layer between the mirrors, ϕ is the phase shift at the edge mirrors, and the product $n_{org} t_{org}$ defines the optical path length through the organic layer at normal incidence. The phase shift ϕ is defined by the optical properties of the organic and metal layers:

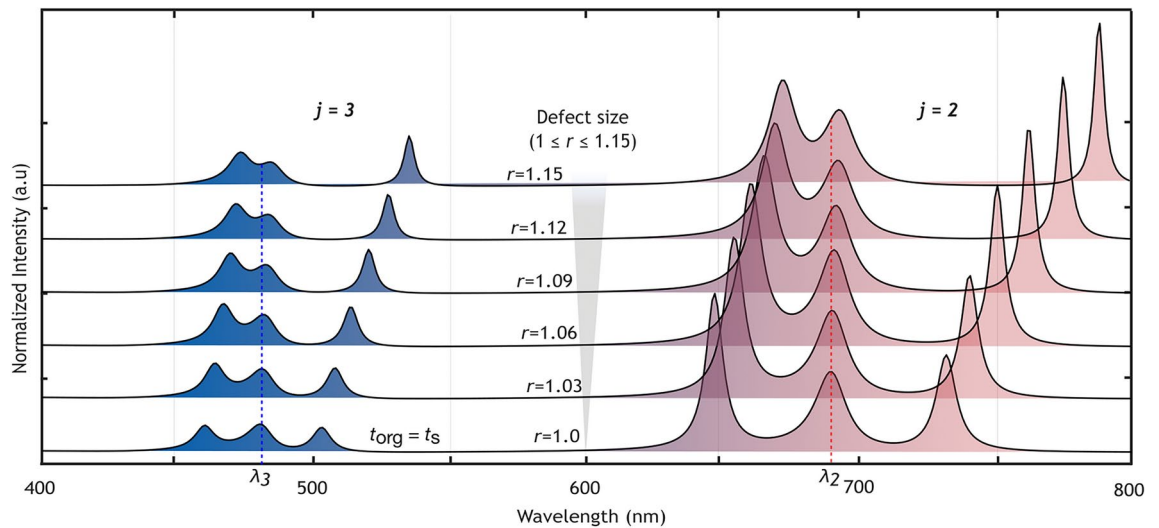$$\phi = \arctan[\frac{n_{org} \, \kappa_m}{n_{org}^2 - n_m^2 - \kappa_m^2}] \qquad (3)$$

Fig. 2. Normalized transmission spectra from Alq_3 for $N = 3$ cavity devices with $r = 1.0, 1.03, 1.06, 1.09,$ 1.12, and 1.15 in the center cavity. Shown here are the second ($j = 2$) and third $j = 3$ bands of states. The three lowest energy states from the fundamental or first band ($j = 1$) have wavelengths far longer than 800nm. The vertical dotted red line roughly at 691 nm and the dotted blue line at 483 nm indicate the centers of the photonic bands for the $j = 2$ and $j = 3$ states in a single microcavity with $t_{org} = t_s$.

Here n_m and κ_m are the real and imaginary parts of the index of refraction for the metals. The two observed photonic bands in Fig. 2 correspond to the $j = 2$ ($\lambda_2 = 691$ nm) and $j = 3$ ($\lambda_3 = 483$ nm) states of a single microcavity with $t_{org} = t_s$.

Similar to the linewidth narrowing of the individual states of a microcavity with increasing j[23], the widths of the photonic bands derived from those states have also been shown to narrow as limiting solutions of the eigenvalues of the transfer matrix.[30] The simulated spectrum in Fig. 2 and the experimental transmission spectrum in Supplementary Fig. 1 confirm this narrowing. The $j = 2$ mode has a bandwidth (defined as the difference between the peak wavelengths of the highest and lowest energy states within the band) of approximately 85 nm, whereas the $j = 3$ mode has a bandwidth of 43 nm.

When a small defect of thickness t_d is introduced in the center cavity of the $N = 3$ MDPC, one of the transmission peaks will exit the photonic band. Figure 2 shows the migration of the defect state out of the band as the magnitude of defect increases to 15% ($1 \leq r \leq 1.15$). As the lowest energy state migrates into the band gap, the linewidth of the defect state decreases and the spacing between the two remaining states is reduced. In the extreme case, the two edge cavities would be uncoupled from the middle cavity and from each other, resulting in degenerate energies identical to the single, uncoupled microcavity. The spacing of states in the photonic band can be controlled by the position of the defect in the crystal. If instead the defect were located in one of the edge cavities, then the extreme case of a defect would leave an isolated defect state and an $N = 2$ coupled resonator system with two distinct states in the band.

These dynamics can be seen more clearly by looking at a larger range of defect sizes. Figure 3 shows the transmission patterns for a full range of defects from $0.02 \leq r \leq 2.0$ for a center cavity defect (a) and an edge cavity defect (b). The horizontal photonic bands at 691 nm and 483 nm correspond to the $j = 2$ and $j = 3$ resonant conditions described above for the static cavity resonator. The vertical dotted white line at $r = 1$ represents the bottom spectrum from Fig. 2. Deviation to the left or right of this line causes one state from each band to migrate into the band-gap leaving two states in the band. In the case of the center cavity defect in Fig. 3a, the two states in the band collapse onto each other becoming nearly degenerate. When the defect is in an edge cavity as in Fig. 3b the remaining states are split, characteristic of a coupled resonator system. The light blue dots in the overlay represent the experimental transmission peak locations. Our results demonstrate a strong agreement between numerical simulations and experimental data; however, the minor discrepancies observed may be attributed to variations between the idealized target thickness of the thin films used in the simulations and the actual thickness of the fabricated films. Deviations of up to $\pm 8\%$ in the thickness of silver films and $\pm 5\%$ in the thickness of Alq_3 films from the target thicknesses were noted in the fabricated MPDC devices. The thicknesses of the Ag mirrors primarily affect the spectral shape and band width due to changes in the unit cell geometry and Peierls distortion[21], whereas the organic (Alq_3) film thickness influences peak and photonic band shifts. The white dashed lines in both panels represent the theoretical transmission peaks described by equation (2), representing the first five resonant wavelengths λ_m, $m = 1, 2, 3, 4, 5$ (left to right) with $t_{org} = t_d$[23]. The defect states generally track these isolated microcavity states except for when the energies of the defect states and the static states overlap $\lambda_m \approx \lambda_j$; a resonance condition to be discussed below.

Examining the transmission spectra and the standing-wave electric field profiles of the resonant states can clarify the underlying mechanisms of the band dynamics. Figure 4a illustrates the normalized transmission
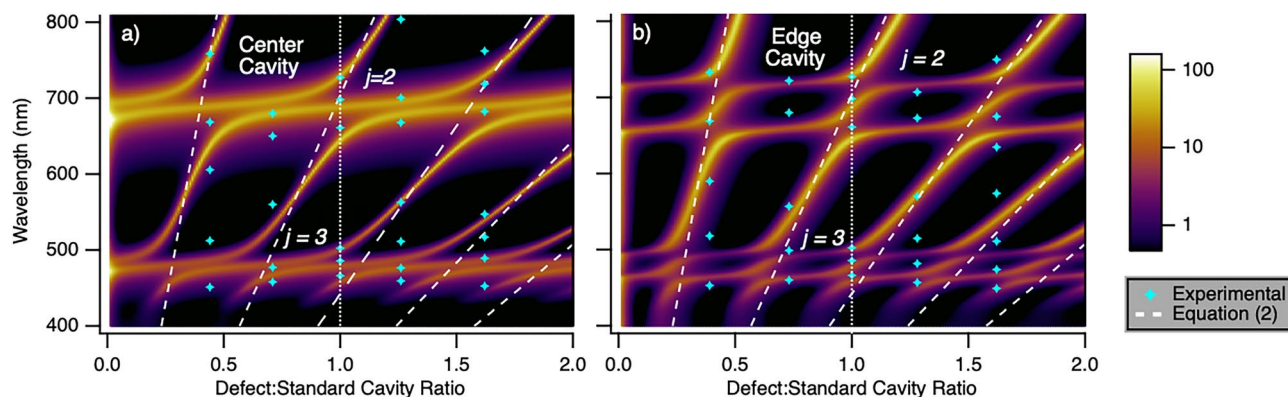
Fig. 3. Computationally simulated (color map) and experimentally resolved transmission spectra for $N = 3$ MDPCs as a function of defect cavity size with $0.02 \leq r \leq 2$ for defect located in (**a**) the center cavity and (**b**) an edge cavity. The vertical white dotted line indicates $r = 1$ (no defect). White dashed lines plot the theoretical transmission peaks described by Eq. (2), for a single, isolated cavity whose size matches the defect cavity.
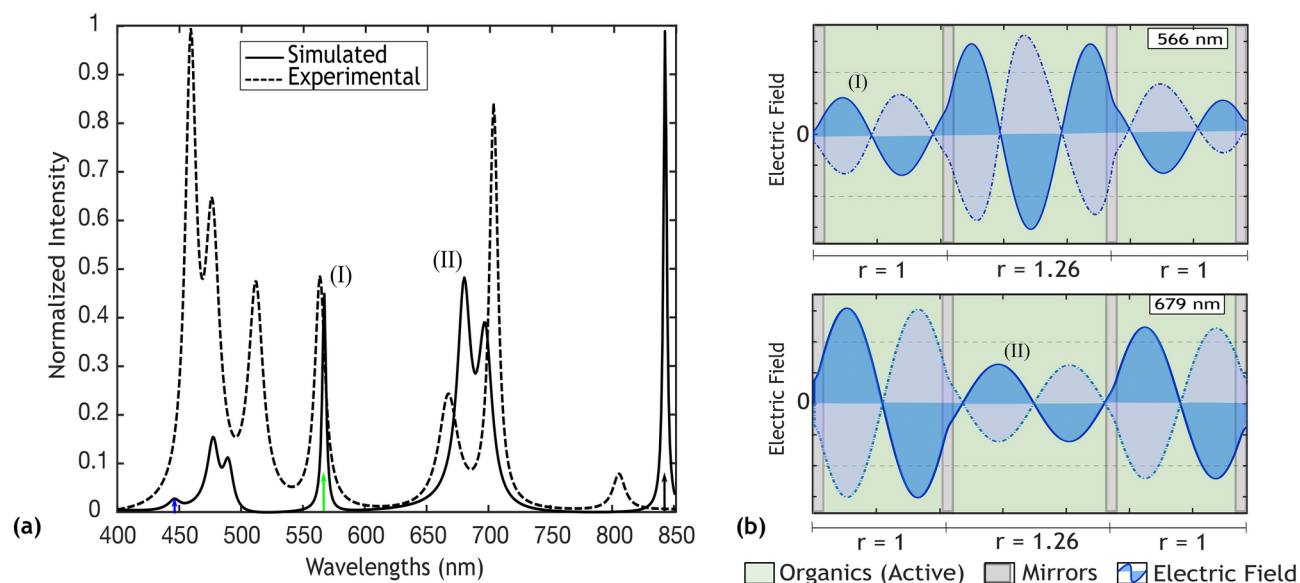

Fig. 4. (**a**) Normalized transmission spectra inside an $N = 3$ MDPC device with the +26% ($r = 1.26$) defect in the center cavity, as determined through computational simulations and experimental measurements. (**b**) Electric field profiles of computationally resolved defect and static states. The energy state approximately at 566nm corresponds to the transmission peak of the defect state and the state at 679nm corresponds to the transmission peak of the static state.

spectra for an $N = 3$ MDPC device, featuring a central cavity defect of +26% ($r = 1.26$), derived from both simulations and experimental observations. The energy peak (blue arrow) near 447 nm and the peak (green arrow) around 566 nm correspond to defect states within the visible spectrum, representing the lowest energy states for the fourth ($j = 4$) and third ($j = 3$) photonic bands, respectively. Additionally, the defect state recorded roughly at 838 nm (black arrow) represents the lowest energy state of the second ($j = 2$) band. In the experimental results, the mid-gap states corresponding to $j = 4$, $j = 3$, and $j = 2$ bands were measured approximately at 457 nm, 561 nm, and 805 nm, respectively. Figure 4b shows the electric field at the wavelength of the defect state (at 566 nm) and the static states (at 679 nm) for a MDPC with center-cavity defect of $r = 1.26$. In the simulation, light originates at dipole emitters located at ten evenly spaced intervals throughout the organic layer. If the organic layer is highlighted green in Figs. 4,5, and 6, then the dipole emitters in that layer are "active" and emitting light into the system. The field amplitude in Fig. 4b indicates that the mid-gap state at 566 nm is localized within the crystal defect while the nearly-degenerate band state at 679 nm is delocalized between the two edge cavities.
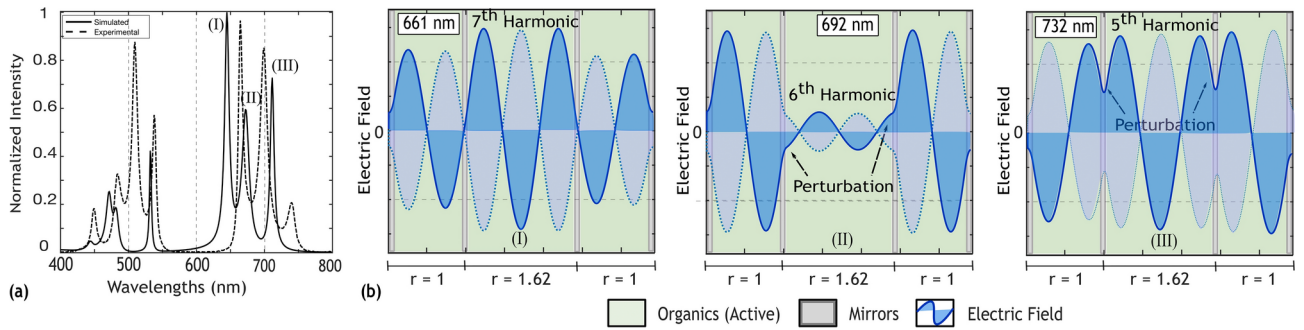
Fig. 5. (**a**) Comparison of simulated and experimental normalized transmission spectra from an $N = 3$ MDPC device at the resonant wavelengths of the states in the second ($j = 2$) band when it has formed a resonant crystal state at +62% ($r = 1.62$) defect in a center cavity and (**b**) corresponding electric field profiles at the resonant wavelengths of the crystal states with three spectral peaks at 661, 692, and 732 nm.
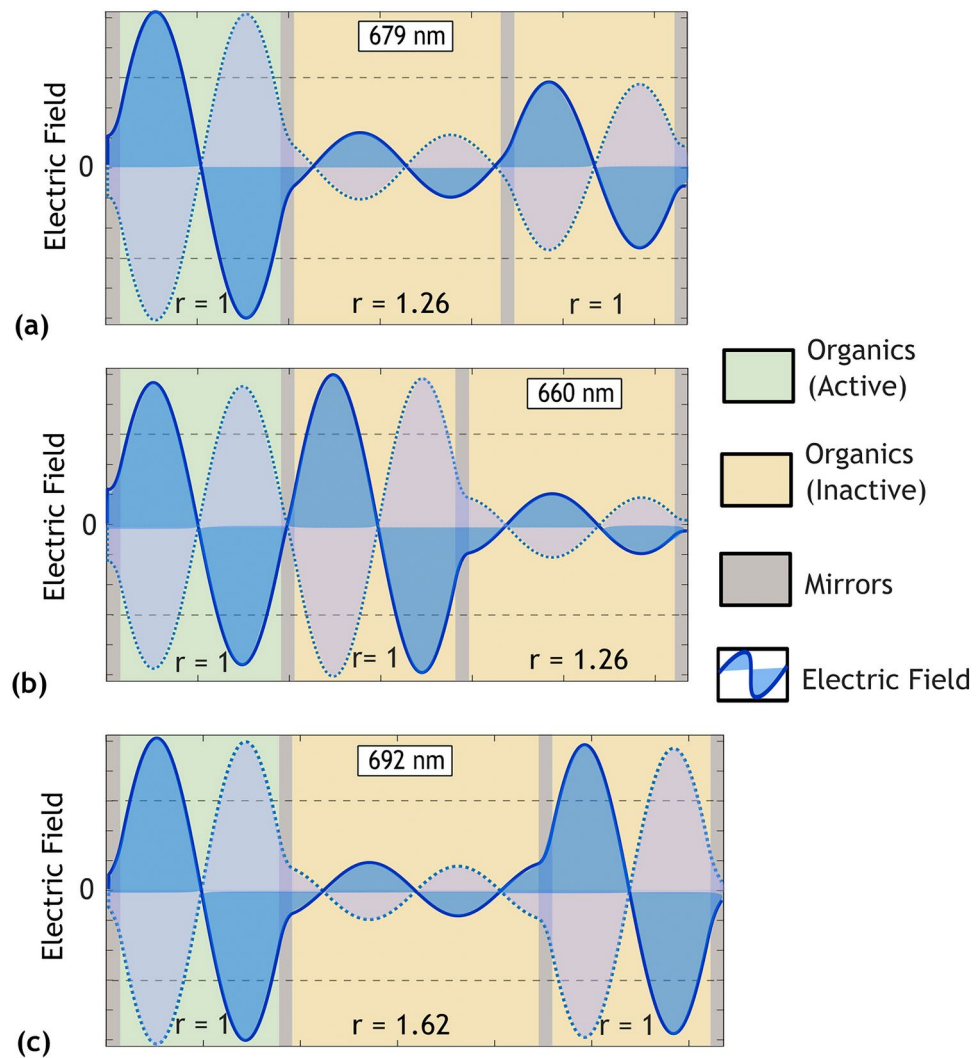

Fig. 6. Electric Field profile concerning only the electric field generated in the left edge (green highlighted) cavity, under the following conditions: (**a**) off-resonance center cavity with defect $r = 1.26$ at a wavelength of 679 nm, (**b**) off-resonance right edge cavity with $r = 1.26$ at 660 nm, and (**c**) on-resonance center cavity with $r = 1.62$ at 692 nm.

Resonant crystal states

The localized states break down as the size of the defect cavity brings it into resonance with one of the existing bands. At this intersection there is an anti-crossing where the defect state rejoins the band to form a "resonant" crystal state like one would see in a device without defects ($r = 1$ case). These resonant crystal states occur with set frequency as the defect is increased or decreased. The resonance condition is determined by $\lambda_j = \lambda_m$:

$$r = \frac{(m - \phi/\pi)}{(j - \phi/\pi)} \tag{4}$$

Resonant crystal states in the second band do not occur at the same magnitude of defect as they do in the third band. Higher energy bands will have more frequent anti-crossings because of the higher j value. In Fig. 3, we observe that, because ϕ is small, the $j = 3$ band has approximately three anti-crossings for every two in the $j = 2$ band. The analogy between this behavior and similar phenomena in quantum mechanics is explored by Zappone et al.[31].

If we consider the case of a defect in the center cavity of an $N = 3$ MDPC, with $r = 1.62$, we see a resonant crystal state as illustrated in Fig. 5. Figure 5a shows the computational and experimental transmission spectra with the formation of a resonant crsytal state in the $j = 2$ band. The resonant crystal state energy peaks at 661, 692, and 732 nm are indicated by (I), (II), and (III). We can see in the Fig. 5b that the standing wave electric field profiles of these three states in the resonant band have 7, 6, and 5 antinodes respectively. One can consider these three resonant states as analogous to the λ_7, λ_6, and λ_5 states of an extended microcavity with thickness $t_{org} = 3.62t_s$. The presence of the two internal mirrors perturbs the wave functions of the λ_6 and λ_5 states significantly more than the λ_7, compressing the states into a band. Therefore, the resonant state condition is determined by the alignment of the mirror positions with nodes in the wave function.[22] Further discussion relating the perturbation of the wave functions and its impact on the energy states is provide in the Supplementary Information.

Communication across defects

The position of the defect, and whether the defect is tuned to resonance with one of the crystal bands, determines the coupling of the two static cavities. We demonstrate this by examining the electric field profiles for several states with only one of the edge cavities active. In Fig. 6a, we see the electric field profile for a center cavity defect with $r = 1.26$ at $\lambda = 679$ nm. The defect is not tuned to resonance, and we can see that the field amplitude in the right edge cavity is significantly suppressed compared to the left. This is particularly striking because the 679 nm wavelength highlighted in 6a represents the peak transmission for both edge cavities. Even though the left edge cavity is generating light at the ideal wavelength for resonance in the right edge cavity, we see very little activity. The exchange of energy is suppressed due to the defect because the off-resonance defect cavity is blocking the transmission of the electromagnetic field. This explains the differences between Fig. 3a,b. Figure 6b shows a similarly off-resonance defect but the $r = 1.26$ defect is in the right edge cavity. The field amplitude at $\lambda = 660$ nm is approximately the same in both of the adjacent static cavities, indicating facile energy exchange and stronger coupling of the resonators. This coupling strength is reflected in the larger splitting of the band states when the edge defect is off resonance. When the center cavity defect is tuned to resonance, as seen in Fig. 6c with $r = 1.62$ and $\lambda = 692$ nm, the field amplitude in both the left and right edge cavities is nearly the same. Therefore, tuning and de-tuning the center cavity defect has significant impact on the coupling strength of the remaining two static cavities.

The thickness of the metal layers between stacked cavities in MDPC structures has been shown to correlate to the density of photonic states in the band. As the coupling between neighboring cavities weakens with increasing metal thickness, the energy states converge to degeneracy.[21] We have found that an off-resonance defect cavity has the same effect when placed between two cavities of the same size, as an off-resonance defect weakens the coupling of the remaining cavities. In this $N = 3$ example, the disruption only occurs if the defect cavity is both off-resonance and located between the standard cavities.

Conclusions

We have shown that the size and location of defects within an MDPC constitute a toolbox for controlling the photonic band structure in sensitive, predictable ways. The ability to create states in the band gap cannot be matched with uniform crystals. We have demonstrated that defects can selectively remove individual states from the set of hybridized states that constitute the photonic band, and that the magnitude of the defect controls the energy of the defect state in the band gap. We have also shown how the location of the defect layer in the stack will determine the degree to which the remaining states in the photonic band become degenerate or remain as distinct energy states. The electric field can be localized in various positions within the crystal structure to enhance the non-linearity of materials for various applications.[32,33] The one-dimensional MDPC structures offer the possibility to tune the photonic dispersion and the corresponding field localization with the relative convenience of fabrication by purely additive processes.[24,34] Our theoretical and experimental framework lays the groundwork for the construction of a novel type of passive optical filters or optoelectronic devices based on OLEDs with finer control over the intensity and spectrum of emitted light.

Data availibility

Data is provided within the manuscript or supplementary information files.

References

1. Ma, G., Tang, S. H., Shen, J., Zhang, Z. & Hua, Z. Defect-mode dependence of two-photon-absorption enhancement in a one-dimensional photonic bandgap structure. *Opt. Lett.* **29**, 1769–1771 (2004).
2. Notomi, M. Theory of light propagation in strongly modulated photonic crystals: Refraction like behavior in the vicinity of the photonic band gap. *Phys. Rev. B* **62**, 10696 (2000).
3. Butt, M., Khonina, S. N. & Kazanskiy, N. Recent advances in photonic crystal optical devices: A review. *Opt. Laser Technol.* **142**, 107265 (2021).
4. Meng, Y. et al. Optical meta-waveguides for integrated photonics and beyond. *Light* **10**, 1–44 (2021).
5. Zhang, Y.-N., Zhao, Y. & Lv, R.-Q. A review for optical sensors based on photonic crystal cavities. *Sens. Actuators A* **233**, 374–389 (2015).
6. Hosseinzadeh Sani, M., Saghaei, H. & Mehranpour, M. . A. A novel all-optical sensor design based on a tunable resonant nanocavity in photonic crystal microstructure applicable in mems accelerometers. *Photonic Sens.* **11**, 457–471 (2021).
7. Koshelev, K. & Kivshar, Y. Dielectric resonant metaphotonics. *Acs Photonics* **8**, 102–112 (2020).
8. Saleh, A. et al. Fifth-order nonlinear optical response of alq3 thin films. *Results Phys.* **37**, 105513 (2022).
9. Mahler, L. et al. Single-mode operation of terahertz quantum cascade lasers with distributed feedback resonators. *Appl. Phys. Lett.* **84**, 5446–5448 (2004).
10. Hill, M. T. & Gather, M. C. Advances in small lasers. *Nat. Photonics* **8**, 908–918 (2014).
11. Smith, N. L., Hong, Z. & Asher, S. A. Responsive ionic liquid-polymer 2d photonic crystal gas sensors. *Analyst* **139**, 6379–6386 (2014).
12. Lonergan, A., Murphy, B. & O'Dwyer, C. Photonic stopband tuning in metallo-dielectric photonic crystals. *ECS J. Solid State Sci. Technol.* **10**, 085001 (2021).
13. Fernández Gavela, A., Grajales García, D., Ramirez, J. C. & Lechuga, L. . M. Last advances in silicon-based optical biosensors. *sensors* **16**, 285 (2016).
14. Lee, W. S., Kang, T., Kim, S.-H. & Jeong, J. An antibody-immobilized silica inverse opal nanostructure for label-free optical biosensors. *Sensors* **18**, 307 (2018).
15. Inan, H. et al. Photonic crystals: Emerging biosensors and their promise for point-of-care applications. *Chem. Soc. Rev.* **46**, 366–388 (2017).
16. Wu, F. et al. Anomalous polarization-sensitive Fabry–Perot resonance in a one-dimensional photonic crystal containing an all-dielectric metamaterial defect. *Opt. Express* **31**, 32669–32683 (2023).
17. Mirshafieyan, S. S., Luk, T. S. & Guo, J. Zeroth order Fabry–Perot resonance enabled ultra-thin perfect light absorber using percolation aluminum and silicon nanofilms. *Opt. Mater. Express* **6**, 1032–1042 (2016).
18. Schuller, J. A. et al. Plasmonics for extreme light concentration and manipulation. *Nat. Mater.* **9**, 193–204 (2010).
19. Pandya, R. et al. Microcavity-like exciton-polaritons can be the primary photoexcitation in bare organic semiconductors. *Nat. Commun.* **12**, 6519 (2021).
20. Caligiuri, V. et al. One-dimensional epsilon-near-zero crystals. *Adv. Photonics Res.* **2**, 2100053 (2021).
21. Allemeier, D. et al. Emergence and control of photonic band structure in stacked oled microcavities. *Nat. Commun.* **12**, 6111 (2021).
22. Allemeier, D. et al. High symmetry metal-dielectric photonic crystal organic light emitting diodes with single-cavity unit cells. *Adv. Opt. Mater.* **11**, 2201631 (2023).
23. Dahal, E., Allemeier, D., Isenhart, B., Cianciulli, K. & White, M. S. Characterization of higher harmonic modes in Fabry–Pérot microcavity organic light emitting diodes. *Sci. Rep.* **11**, 8456 (2021).
24. Allemeier, D., & White, M. S. Parametric investigation of ideal metal-dielectric photonic crystals. In *Organic and Hybrid Light Emitting Materials and Devices XXVI*, vol. 12208 29–34 (SPIE, 2022).
25. Pawlak, D. A. Metamaterials and photonic crystals–potential applications for self-organized eutectic micro-and nanostructures. *Scientia Plena* **4** (2008).
26. Ma, G. et al. Optimization of two-photon absorption enhancement in one-dimensional photonic crystals with defect states. *Appl. Phys. B* **80**, 359–363 (2005).
27. Lee, K. J., Wu, J. & Kim, K. Defect modes in a one-dimensional photonic crystal with a chiral defect layer. *Opt. Mater. Express* **4**, 2542–2550 (2014).
28. Popczyk, A. et al. Selected organometallic compounds for third order nonlinear optical application. *Nanomaterials* **9**, 254 (2019).
29. Dodabalapur, A. et al. Physics and applications of organic microcavity light emitting diodes. *J. Appl. Phys.* **80**, 6954–6964 (1996).
30. Allemeier, D. & White, M. S. Quasinormal modes and coupled mode theory of 1d metal-dielectric photonic crystals. *Nano Select* **2014**, e2300122 (2024).
31. Zappone, B., Caligiuri, V., Patra, A., Krahne, R. & De Luca, A. Understanding and controlling mode hybridization in multicavity optical resonators using quantum theory and the surface forces apparatus. *ACS Photonics* **8**, 3517–3525 (2021).
32. Soljačić, M. & Joannopoulos, J. D. Enhancement of nonlinear effects using photonic crystals. *Nat. Mater.* **3**, 211–219 (2004).
33. Zanotto, S., Biasiol, G., Sorba, L. & Tredicucci, A. Photonic bands and defect modes in metallo-dielectric photonic crystal slabs. *JOSA B* **31**, 1451–1455 (2014).
34. Hattori, T., Tsurumachi, N. & Nakatsuka, H. Analysis of optical nonlinearity by defect states in one-dimensional photonic crystals. *JOSA B* **14**, 348–355 (1997).

Acknowledgements

Author contributions

K.S.T., T.C., and M.S.W. wrote and edited the manuscript text and prepared the figures. D.A. developed the computational modeling tool. K.S.T and T.C customized the transfer matrix program and performed all optical simulations. M.S.W. and K.S.T. developed the experimental procedures. K.S.T. fabricated and characterized the MDPC devices. K.S.T, T.K, K.N, N.A, and A.M conducted experiment. K.S.T., T.C., D.A., and M.S.W. analysed the results. M.S.W. conceived and supervised the project. All authors reviewed the manuscript.

Declarations

Competing interests
M.S.W. and D.A. are inventors on PCT Patent Application No. PCT/US21/71679 with the University of Vermont and State Agricultural College as applicant. This patent covers light emitting devices with coupled resonant photonic unit cells.

Additional information
Supplementary Information The online version contains supplementary material available at https://doi.org/10.1038/s41598-024-78971-6.

Correspondence and requests for materials should be addressed to M.S.W.

Reprints and permissions information is available at www.nature.com/reprints.

Publisher's note Springer Nature remains neutral with regard to jurisdictional claims in published maps and institutional affiliations.